Experimental Evaluation of Haptic Shared Control for Multiple Electromagnetic Untethered Microrobots

Marco Ferro, Franco N. Piñan Basualdo, Paolo Robuffo Giordano, *Senior Member, IEEE*, Sarthak Misra, *Senior Member, IEEE*, and Claudio Pacchierotti, *Senior Member, IEEE*

Abstract— The precise manipulation of microrobots presents challenges arising from their small size and susceptibility to external disturbances. To address these challenges, we present the experimental evaluation of a haptic shared control teleoperation framework for the locomotion of multiple microrobots, relying on a kinesthetic haptic interface and a custom electromagnetic system. Six combinations of haptic and shared control strategies are evaluated during a safe 3D navigation scenario in a cluttered environment. 18 participants are asked to steer two spherical magnetic microrobots among obstacles to reach a predefined goal, under different conditions. For each condition, participants are provided with different obstacle avoidance and navigation guidance cues. Results show that providing assistance in avoiding obstacles guarantees safer performance, regardless if the assistance is autonomous or delivered through a haptic repulsive force. Moreover, autonomous obstacle avoidance also reduces the completion time by 30% compared to haptic obstacle avoidance and no obstacle avoidance cases, although haptic feedback is preferred by the users. Finally, providing haptic guidance towards the target improves by the 65% the positioning accuracy of the microrobots with respect to not providing this guidance. We also present some illustrative scenarios to generalize the presented haptic shared control strategies to arbitrary formations of N microrobots, while showing the effectiveness of the method for a clinical use-case of endovascular navigation in simulated environment.

Note to Practitioners—The recent increasing interest in microrobotics arises from its potential applications in fields like medicine, manufacturing, and environmental monitoring, enabling highly precise control of minimally invasive tools. By enabling users to teleoperate microscale tools with partial autonomous support, these systems facilitate safe access to confined spaces, enhance task efficiency, and enable navigation in otherwise inaccessible environments. Our presented solution serves as an experimental platform to evaluate the efficacy of different combinations of tactile feedback and partial autonomy during safe navigation tasks, with potential applications spanning microsurgery, drug delivery, microscale manufacturing, and environmental remediation. Further practical adaptation of the system will require defining specific application objectives and specifications, along with potential modifications to the actuation system to accommodate environmental constraints of targeted scenarios.

Index Terms— Haptics and haptic interfaces, telerobotics and teleoperation, micro/nano robots.

I. INTRODUCTION

IN THE rapidly evolving landscape of microscale robotics, the manipulation of untethered magnetic microrobots has emerged as a versatile frontier, finding applications in domains ranging from microscale assembly [1] to environmental monitoring [2] and clinical scenarios [3], [4], [5]. In such situations, magnetic microrobots navigate complex environments at a submillimeter scale, encountering significant challenges related to precision, stability, situational awareness, and reliable control [6], [7].

Fully automated control strategies have gathered attention in recent research [8], [9], [10]. However, these approaches often require precise environmental knowledge, which is challenging in dynamic, complex scenarios. As an alternative, *shared control* strategies combine human intuition with the precision of autonomous systems, being ideal for tasks requiring adaptability, such as navigating intricate biological structures or reacting to unexpected scenarios [11], [12], [13].

Incorporating human oversight into the control loop ensures the operator can intervene when necessary, thus enhancing system safety and reliability. Shared control has proven effective across diverse fields, including driver-assistance technologies [14], collaborative robots in industrial automation [15], and medical robotics for surgical, rehabilitation, and assistive purposes [16], [17], [18]. Specifically in the medical field, where microrobotic systems often operate in complex, unpredictable environments [19], human intervention can address sensing limitations and improve decision-making [5].

Moreover, shared control can allow microrobots to adapt to various tasks without extensive reprogramming, providing flexibility that fully autonomous systems lack.

Shared control is also particularly advantageous for managing robotic systems with high degrees of freedom (DoFs) [20], [21], where direct control would be time-consuming and mentally taxing. Haptic feedback in shared control enhances situational awareness by providing operators with tactile cues about the autonomous controller's actions. This approach has been applied in guiding robots along trajectories [22], [23], [24], assisting in manipulation [21], [25], and ensuring safe navigation in cluttered environments. Techniques like dynamic windows [26], formation maintenance [27], Model Predictive Control [28], and potential fields [29] are used to maintain safe paths. Among these, potential fields are favored for their simplicity, computational efficiency, and real-time performance in haptic shared control [29], [30], [31].

Despite the promising application scenarios, the use of such advanced control techniques is rather limited, especially for controlling untethered multirobot systems [32]. For example, Lucarini et al. [33] presented a magnetic navigation platform for lab-on-a-chip applications using one microrobot. Pacchierotti et al. [34] presented a haptic teleoperation system to control the positioning of a self-propelled microjet in 2D. Zhang et al. [35] designed a haptic teleoperation framework for the control of a magnetic 3-dimensional microrobot utilizing micro-assembly of out-of-plane compliant mechanical structures, employed in microsized navigation and transportation [36], [37]. Pacchierotti et al. [38] evaluated a haptic teleoperation system for the control of an untethered small-scale soft gripper in microtransportation tasks; the system can move and open/close the grippers by regulating the magnetic field and temperature in the workspace. Furthermore, controlling *multiple* robots at the microscale is potentially decisive for tasks requiring high manipulability and redundancy capabilities, while it also poses additional challenges. In this respect, enabling *independent* control of multiple microrobots is a desirable feature that would improve their deployment in complex and inaccessible environments, e.g., within the human body for targeted therapy or diagnostic purposes [39]. Chowdhury et al. [40] depicted the main approaches in multiple microrobots control, highlighting the necessity of developing dedicated control algorithms. Gerena et al. [41] developed a telerobotic platform for optical manipulation of multiple cells or microrobots. Basualdo et al. [42] developed a thermocapillary platform capable of manipulating multiple agents. Kawaguchi et al. [43] proposed a magnetic actuation system enabling independent 2D control of two helical micromagnetic actuators. Finally, a survey highlighting recent developments about multiple microrobots systems for *in vitro* applications can be found in [44].

However, to the best of our current knowledge, there are no existing haptic-enabled teleoperation systems that facilitate the intuitive control of multiple microrobots simultaneously. Within this perspective, this paper proposes a haptic-enabled shared control framework for microrobotics, shown in Fig. 1, focusing on its experimental evaluation with human subjects. The framework exploits the system proposed in [45] to achieve
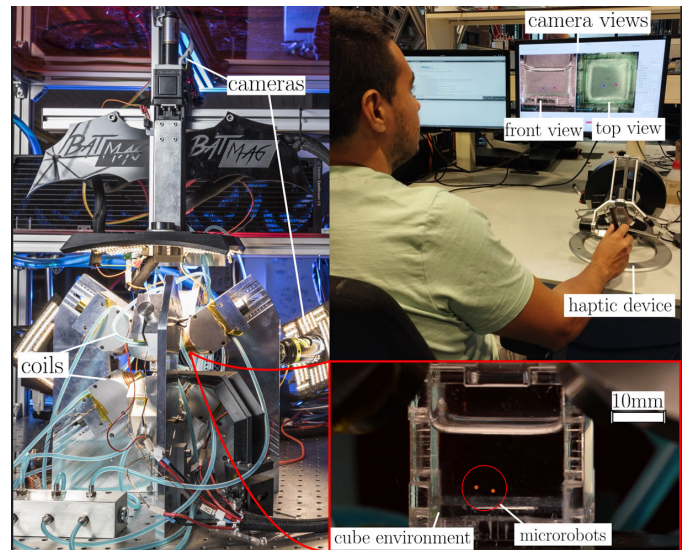

Fig. 1. Experimental setup. (Left) The BatMag system enables independent 3D control of a pair of microrobots through the actuation of nine electromagnetic coils. (Top Right) An Omega.6 grounded kinesthetic haptic interface (Force Dimension, CH) enables the human user to control the coordinated motion of the two microrobots, aided by the proposed haptic shared control techniques.

independent control of a pair of electromagnetic microrobots, integrating shared control techniques and haptic feedback in the control paradigm. The proposed shared control integrates the specific challenges of the magnetic control of microrobots, related to the physical constraints (e.g., maintain a safe minimum distance to prevent mutual magnetic attraction between microrobots) and implementation particularities (e.g., limited perception of the microscaled workspace). Our contributions include:

- Design of a teleoperation system for controlling pairs of electromagnetic microrobots in a shared control framework, i.e., being able to jointly combine the experience of the human user with the accuracy and robustness of an autonomous algorithm;
- shared control and haptic feedback strategies for a representative scenario of safe navigation in 3D cluttered environments, designed so as to consider the constraints and specificities of the microrobotic system at hand[1];
- Human subject user study evaluation, investigating the role and effectiveness of different combinations of shared control and haptic strategies in the considered 3D navigation scenario.

Finally, we also demonstrate the versatility of the proposed methodology through illustrative scenarios, including its extension to N-microrobot formations and its application in a clinical use case involving safe navigation within a simulated endovascular environment.

II. EXPERIMENTAL METHODS

The proposed teleoperation system exploits the electromagnetic setup for independent 3D control of microrobots

---

[1]By *safe* navigation, we mean the capability of the microrobots to navigate without generating collisions among each others or against elements of the surrounding environment.
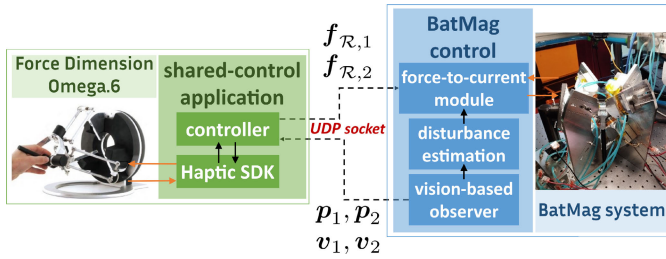
Fig. 2. Architecture of the haptic teleoperation system. The control system is divided between two computers that communicate through a UDP socket. The first computer, connected to the Omega.6 device, runs the shared control application which computes the required forces for moving the robots ($\mathbf{f}_{\mathcal{R},1}$, $\mathbf{f}_{\mathcal{R},2}$). The second computer, connected to the BatMag electromagnetic system, tracks the motion of the particles, specified through the position and velocity variables $(\boldsymbol{p}_1, \boldsymbol{p}_2, \boldsymbol{v}_1, \boldsymbol{v}_2)$, and computes the required currents to move them.

BatMag [45]. With respect to the original BatMag setup, we replaced the embedded autonomous control with a shared control paradigm, combining the users' inputs registered by an Omega.6 grounded haptic interface with those of an autonomous control algorithm. In addition, the Omega.6 also provides the user with haptic feedback conveying additional information about the teleoperation strategy. This architecture is summarized in Fig. 2. The details of the different parts of this architecture are described in the following subsections.

A. The BatMag System

The BatMag electromagnetic system, shown in Figs. 1-left and 3a, allows independent 3D control of pairs of identical and non-identical spherical microrobots, from 250 μm to 1 mm of radius. The motion of the microrobots is induced by magnetic fields and gradients generated by nine electromagnetic coils, positioned to satisfy specific workspace accessibility and force exertion constraints. In this work, the microrobots (0.5 mm diameter AISI 420C stainless steel spheres) navigate in a $22 \times 22 \times 22$ mm cubic workspace, filled with silicone oil M 1000 (density 0.98 g/cm^3, viscosity 1000 cSt). At its center, the system can generate magnetic field flux and gradients up to 160 mT and 3.6 T/m, respectively. An example of the generated magnetic field distribution for the levitation and actuation of two microrobots is shown in Fig. 4.

Two cameras, placed on the top and right-hand side of the workspace (see Figs. 1 and 3a), show the remote environment to the user, as visible in Fig. 5 (virtual obstacles are superposed to these images, see Sec. IV-A). The same images are also used by a vision-based observer to track the position and velocity of the pair of microrobots, namely $(\boldsymbol{p}_1, \boldsymbol{p}_2, \boldsymbol{v}_1, \boldsymbol{v}_2)^T$, and estimate force disturbances. The high magnification of the lenses minimizes perspective distortion in the workspace, which is beneficial for the precision of the implemented stereo tracking system. However, this hinders the user's cognitive interpretation of the images since the lack of perspective can make depth perception and spatial comprehension more difficult, especially when virtual obstacles are superposed on the images.

The communication module receives the forces $\boldsymbol{f}_{\mathcal{R},1}, \boldsymbol{f}_{\mathcal{R},2}$ that the system should apply on each i-th microrobot, for $i = 1, 2$, according to the considered control technique. These

magnetic force are related to the set of currents $\boldsymbol{I}$ of the electromagnetic coils through the relationship

$$\boldsymbol{f}_{\mathcal{R},i} = K_{\text{mag}} \, \nabla \mathbf{B}(\boldsymbol{p}_i, \boldsymbol{I}) \cdot \mathbf{B}(\boldsymbol{p}_i, \boldsymbol{I}) \tag{1}$$

where $\mathbf{B}$ is the magnetic field and $K_{\text{mag}} = \pi \frac{d^3}{\mu_0}$ is the sphere's magnetization constant, being μ_0 the vacuum magnetic permeability and d the sphere diameter. For a desired magnetic force, the corresponding currents $\boldsymbol{I}$ to inject to the electromagnetic coils are found by numerically solving eq. (1) subject to the constraints $|I_j| \leq 5 \, \text{A} \, \forall j$ to avoid overheating of the coils, utilizing a model-based optimization routine [1]. Autonomous independent control of two magnetic microspheres is achieved in 3-dimensional space with average steady-state errors of 30 μm and peak velocities of up to 1.4 mm/s.

B. The Omega.6 Haptic Device

The Omega.6 (Force Dimension, CH), shown in Fig. 3b, is a 6-DoF kinesthetic haptic interface. The measured Cartesian coordinates of the end-effector are used to set the 3D reference position of the centroid of the pair of controlled microrobots (see also Sec. II-C). Furthermore, the rotations of the fourth (J_4 in Fig. 3b) and sixth (J_6) joint are used to alternatively control, through a click of the button, the orientation angles ϕ and θ of the pair of robots around the y and z axes of the BatMag environment, respectively. This design choice is due to the imaging system of the BatMag electromagnetic actuation platform, that does not provide a complete 3D visualization of the target environment, but a separate visualization of the two 2D views from the orthogonal cameras. The mapping is depicted in Figs. 3b and 3a by matching the reference frames $\mathcal{F}_H$ and $\mathcal{F}_B$ in the human and BatMag remote environments, respectively. Finally, the three active degrees of freedom are used to provide haptic cues. In the navigation scenario considered in this paper, we provide the user with repulsive forces to avoid obstacles and/or attractive guidance forces to reach the assigned goal.

C. Microrobots Teleoperation

To achieve teleoperation control, the proposed architecture interconnects the BatMag and the Omega.6 haptic device over a User Datagram Protocol (UDP) connection, as summarized in Fig. 2. On one side, the current positions and velocities of the pair of microrobots $(\boldsymbol{p}_1, \boldsymbol{p}_2, \boldsymbol{v}_1, \boldsymbol{v}_2)^T$, sensed by the vision-based observer module of the BatMag system, are forwarded to the external control application. On the other side, the application handles the communication with the haptic device and generates the force control inputs $\boldsymbol{f}_{\mathcal{R},1}$ and $\boldsymbol{f}_{\mathcal{R},2}$ (one per robot) to be forwarded to the BatMag system to compute the required currents. The reference frame $\mathcal{F}_B$, attached to the BatMag system, is assumed to be positioned at the bottom surface of cube environment,[2] and oriented as shown in Figs. 3a-3c and 5. Similar to the approach in [46], the BatMag control system incorporates a disturbance estimation module that leverages the microrobots' measured motion to estimate force disturbances in the actuation system and compensate for them.

---

[2]Unless otherwise specified with a proper superscript, variables are from now on assumed to be expressed with respect to $\mathcal{F}_B$.

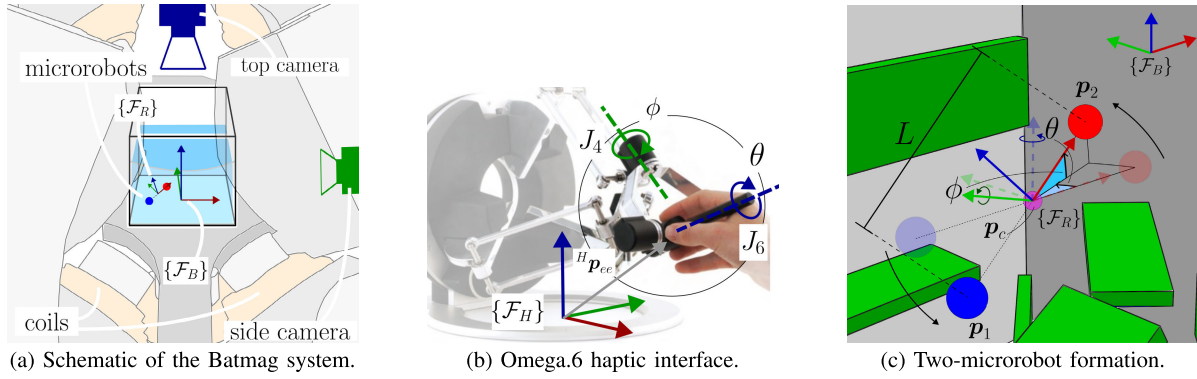(a) Schematic of the Batmag system.   (b) Omega.6 haptic interface.   (c) Two-microrobot formation.

Fig. 3. (a) Rendering of the BatMag electromagnetic setup. The pair of microrobots (red and blue spheres) identifies the reference frame $\mathcal{F}_R$ and moves in a cubic workspace positioned in between the coils identified by the reference frame $\mathcal{F}_B$. The cameras are positioned on the side and top of the 3D environment. (b) The translation $^H\boldsymbol{p}_{ee}$ of the Omega.6 end-effector in $\mathcal{F}_H$ enables the teleoperation of the centroid position of the pair of microrobots, while the rotation of joints J_4 and J_6 sets the orientation (θ, ϕ) of the pair. (c) The formation of the pair of microrobots, with positions $\boldsymbol{p}_1$ and $\boldsymbol{p}_2$, is specified by their centroid ($\boldsymbol{p}_c$), the orientation angles (θ, ϕ), and the relative distance (L). The green cuboids represent the virtual obstacles.
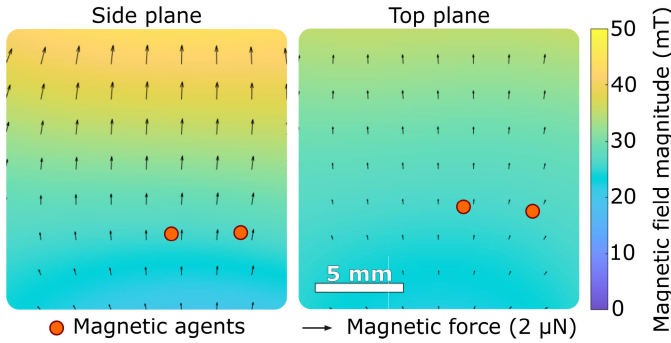

Fig. 4. Magnetic field generated by the BatMag system to levitate and displace two magnetic particles. The colormap represents the magnetic field magnitude on the side (x–z) and top (x–y) planes. The arrows represent magnetic force.
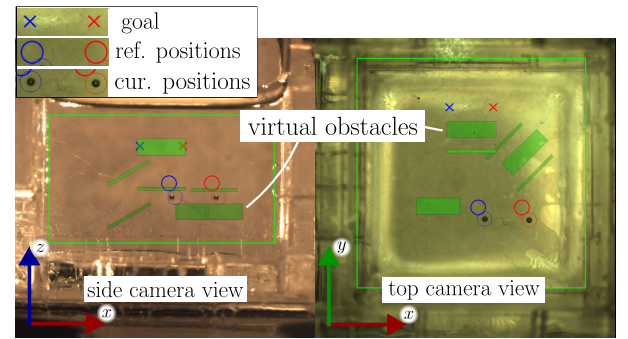

Fig. 5. Camera views of the 3D remote environments, as shown to the user. The virtual obstacles are superposed on the images. The goal, target reference (ref.) positions for the microrobots, and their current (cur.) tracker positions are highlighted by colored crosses, thick circles, and thin circles, respectively.

The teleoperation is designed to map the motion of the haptic device to a reference robot *formation* $F_d = \langle \boldsymbol{p}_c, \phi, \theta, L \rangle$, that identifies the reference frame $\mathcal{F}_R$ (see also Fig. 3c), where: $\boldsymbol{p}_c = \frac{1}{2}(\boldsymbol{p}_1 + \boldsymbol{p}_2)$ is the position of the *centroid* point between the two microrobots, i.e., the middle point of the segment linking the two microrobots and the origin of $\mathcal{F}_R$; θ and ϕ are the rotation angles of the segment $(\boldsymbol{p}_2 - \boldsymbol{p}_1)$ connecting the two microrobots, generated around the *fixed* axis z of $\mathcal{F}_B$ and the *moving* axis $-y$ of $\mathcal{F}_R$, respectively[3] (for $\theta = \phi = 0$, $\mathcal{F}_R$ is oriented as $\mathcal{F}_B$); and $L = \|\boldsymbol{p}_2 - \boldsymbol{p}_1\|$ is the relative distance between the two microrobots. The three translational DoFs of the haptic interface, shown in Fig. 3b, are used to map the end-effector position to the centroid position $\boldsymbol{p}_C$, while the roll and yaw rotational DoFs (J_4 and J_6 in Fig. 3b) are mapped to the orientation angles ϕ and θ, respectively (see also Fig. 3c). Only one rotation at a time is enabled, with the switching between the two rotations done through the end-effector button of the Omega.6 interface.

The position and the velocity $(^H\boldsymbol{p}_{ee}, {}^H\boldsymbol{v}_{ee})^T$ of the Omega.6 end-effector determine the desired position and velocity $(\boldsymbol{p}_{c,d}, \boldsymbol{v}_{c,d})^T$ of the centroid point of the robotic formation:

$$\begin{pmatrix} \boldsymbol{p}_{c,d} \\ \boldsymbol{v}_{c,d} \end{pmatrix} = \boldsymbol{S}_t \; {}^B\bar{\boldsymbol{R}}_H \begin{pmatrix} {}^H\boldsymbol{p}_{ee} + \boldsymbol{l}_{H,min} \\ {}^H\boldsymbol{v}_{ee} \end{pmatrix}, \qquad (2)$$

where $\boldsymbol{S}_t = \boldsymbol{S}_t(\boldsymbol{l}_{H,min}, \boldsymbol{l}_{H,max}, \boldsymbol{l}_B) \in \mathbb{R}^{6\times 6}$ is a diagonal scaling matrix that scales the device end-effector motion from

the Omega workspace $[\boldsymbol{l}_{H,min}, \boldsymbol{l}_{H,max}]$ to that of the BatMag $[-\boldsymbol{l}_B/2, \boldsymbol{l}_B/2]$, while ${}^B\bar{\boldsymbol{R}}_H = \text{diag}({}^B\boldsymbol{R}_H, {}^B\boldsymbol{R}_H)$ with ${}^B\boldsymbol{R}_H \in SO(3)$ denotes the rotation matrix of the relative orientation of $\mathcal{F}_H$ with respect to $\mathcal{F}_B$.

Similarly, the desired orientation of the microrobotic formation, denoted by angles ϕ_d and θ_d, is set as $(\phi_d, \theta_d)^T = \boldsymbol{S}_r(\boldsymbol{\psi}_{H,min}, \boldsymbol{\psi}_{H,max})(q_4, q_6)^T$, where $\boldsymbol{S}_r \in \mathbb{R}^{2\times 2}$ is a diagonal scaling matrix that normalizes the Omega.6 joint rotation values $(q_4, q_6)^T$ of J_4 and J_6, from the workspace $[\boldsymbol{\psi}_{H,min}, \boldsymbol{\psi}_{H,max}]$ of the haptic device to the admissible range of rotations $[-\pi, \pi]$ around the formation rotation axes.

Hence, for a desired relative distance L_d, the corresponding desired positions for the two microrobots are then set as

$$\boldsymbol{p}_{1,d} = \boldsymbol{p}_{c,d} - \frac{L_d}{2}(c_{\phi_d}c_{\theta_d}, c_{\phi_d}s_{\theta_d}, s_{\phi_d})^T$$

$$\boldsymbol{p}_{2,d} = \boldsymbol{p}_{c,d} + \frac{L_d}{2}(c_{\phi_d}c_{\theta_d}, c_{\phi_d}s_{\theta_d}, s_{\phi_d})^T \qquad (3)$$

with c_* and s_* denoting *cos* and *sin* functions, respectively.

Finally, the force contribution to teleoperate each microrobot i is given by

$$\boldsymbol{f}_{\mathcal{T},i} = K_p(\boldsymbol{p}_{i,d} - \boldsymbol{p}_i) + K_v(\boldsymbol{v}_{i,d} - \boldsymbol{v}_i) \qquad (4)$$

being $\boldsymbol{v}_{i,d} = \dot{\boldsymbol{p}}_{i,d}$, with $K_p, K_v \geq 0$. This force $\boldsymbol{f}_{\mathcal{T},i}$ is possibly combined with other contributions, depending on the selected shared control behavior (see below), to determine the ultimate control inputs that will be transmitted to the BatMag system to control the two microrobots.

[3]For $\varphi = \phi - \frac{\pi}{2}$, the pair (φ, θ) corresponds to the polar and azimuthal angles of the equivalent spherical coordinate system.

D. Digital Twin System

In the final architecture design, we leveraged the CoppeliaSim simulation software[4] to create a virtual environment that faithfully replicates the real workspace of the BatMag system, as shown in Fig. 6. This virtual scene serves as a *digital twin*, offering a 3D, enhanced, navigable visualization of the real microscale environment and system state, reconstructed from available sensors. The digital twin also provides additional features that can enhance the operator's situational awareness during task execution, such as real-time signal monitoring and augmented feedback, thus significantly improving the human operator's perception of the environment.

Moreover, the virtual environment can also serve as standalone simulator, allowing to overcome the sensing and actuation limitations of the real system, enabling to test, validate, and generalize the designed control strategies in a wider set of settings and environments. This potential will be further presented and discussed in Sect. V and Sect. VI.

III. SHARED CONTROL AND HAPTIC STRATEGIES FOR 3D NAVIGATION IN CLUTTERED ENVIRONMENTS

As a representative example of haptic-enabled shared control in the context of multi-robot control at the micro-scale, we considered the steering of two microrobots in a 3-dimensional environment cluttered with obstacles. For this purpose, the cubic workspace of the BatMag system is populated with virtual rectangular prismatic obstacles at arbitrary locations, as shown in Figs. 5 and 6.

Our shared control algorithm is designed to help the human user safely steer the two untethered microrobots across the cluttered workspace toward a predefined goal. To do so, the designed algorithm integrates the teleoperation control, detailed in Sec. II-C, with two further complementary components: i) obstacle and mutual avoidance, allowing the user to safely move the microrobots throughout the workspace avoiding collisions with the obstacles and with each other (see Sec. III-A); and ii) navigation guidance, leading the user towards the target goal (see Sec. III-B). Our experiment aims to evaluate the role of these different components and their rendering techniques in the performance and user experience of the considered task.

A. Obstacle and Mutual Avoidance

The obstacle avoidance strategy is based on the definition of potential field functions. The virtual obstacles are first discretized in a fine set of $N_{\mathcal{O}}$ points with positions $\boldsymbol{p}_{\mathcal{O}_j}$, $j = 1, \ldots, N_{\mathcal{O}}$. Then, for a generic robot agent with position $\boldsymbol{p}$, a potential field function can be defined as

$$g(\boldsymbol{p}) = \sum_{j=1}^{N_{\mathcal{O}}} e^{-\alpha \|\boldsymbol{p} - \boldsymbol{p}_{\mathcal{O}_j}\|_2}, \tag{5}$$

with $\alpha > 0$. A repulsive force contribution $\boldsymbol{f}_{\mathcal{O},i}$ that allows to move away from the obstacles is then evaluated as proportional to the gradient of the potential function (5),

$$\boldsymbol{f}_{\mathcal{O},i}(\boldsymbol{p}, \boldsymbol{v}) = -\rho_{\mathcal{O}} \nabla g(\boldsymbol{p}), \tag{6}$$

[4]https://www.coppeliarobotics.com/
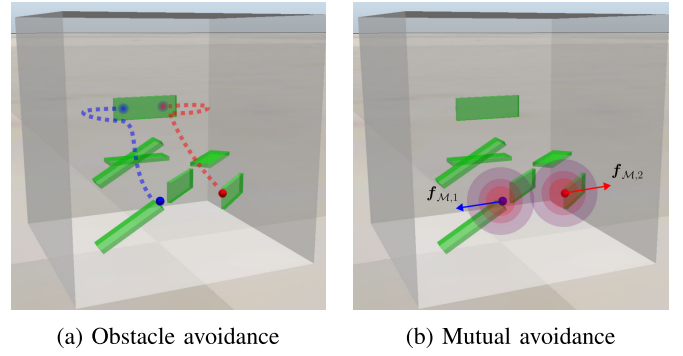

(a) Obstacle avoidance   (b) Mutual avoidance

Fig. 6. Calculation of additional forces exerted on the microrobots (blue and red spheres). (a) The obstacle avoidance contribution is computed as a function of the distance to the obstacles (green cuboids). (b) The mutual avoidance contribution is computed as a function of the distance between the microrobots. Arrows indicate the direction of the mutual repulsive force component $\boldsymbol{f}_{\mathcal{M},i}$.

where $\boldsymbol{v} = \dot{\boldsymbol{p}}$, while $\rho_{\mathcal{O}} > 0$ is a repulsive proportional gain. A representative trajectory resulting from the obstacle avoidance strategy is shown in Fig. 6a.

A similar strategy is implemented to avoid *mutual* collisions between the two microrobots. Indeed, when microrobots come within a critical distance of each other, dipole-dipole magnetic interactions may occur, potentially causing the pair to collapse. In this case, we consider the following potential field function of the current microrobots positions $\boldsymbol{p}_i$:

$$g_{\mathcal{M}}(\boldsymbol{p}_i) = \frac{1}{2} e^{-\alpha \|\boldsymbol{p}_i - \boldsymbol{p}_j\|_2}, \quad i = 1, 2, \quad i \neq j \tag{7}$$

and the resulting mutual avoidance force contribution is

$$\boldsymbol{f}_{\mathcal{M},i} = -\rho_{\mathcal{M}} \nabla g_{\mathcal{M}}(\boldsymbol{p}_i), \tag{8}$$

for $\rho_{\mathcal{M}} > 0$. A representation of the force contribution resulting from the mutual avoidance strategy is shown in Fig. 6b.

We also stress that the minimum safe distance between robots, guaranteeing that magnetic dipole-dipole interactions do not cause the pair to collapse, depends on the characteristics of the actuation system. Indeed, the magnitude of the magnetic dipole-dipole interaction force is

$$|\boldsymbol{f}_{\text{dip-dip}}| = \frac{3 \, \mu_0 \, K_{\text{mag}}^2 \, |\mathbf{B}|^2}{2 \, \pi \, r^4}, \tag{9}$$

where r is the distance between the particles. On the other hand, being the magnetic gradient force exerted on the particle given by eq. (1), we can compute the critical distance below which the magnetic dipole-dipole interaction dominates the applied magnetic gradient force as

$$r_{\text{crit}} = d \sqrt[4]{\frac{3 \, |\mathbf{B}|^2}{2 \, d \, |\nabla \mathbf{B} \cdot \mathbf{B}|}}. \tag{10}$$

For utilized values ($|\mathbf{B}| \approx 20 \, \text{mT}$, $|\nabla \mathbf{B} \cdot \mathbf{B}| \approx 0.1 \, \text{T/m}^2$, and $d = 0.5 \, \text{mm}$) $r_{\text{crit}} \approx 1 \, \text{mm}$. However, the minimum stable distance is expected to be larger than r_{crit} since, when the microrobots are close to each other, the capability of the electromagnetic system of applying opposing forces on the particles is reduced. To prevent this from occurring, the parameter α, which defines the mutual avoidance artificial potential in eq. (7), is empirically adjusted.

B. Navigation Guidance

To help the user reaching the considered goal formation configuration F_g, we also consider a navigation guidance technique, combining conical (a) and paraboloidal (b) cost functions to guide the microrobots towards the goal:

$$\mathcal{J} = \begin{cases} k_{\mathcal{G},a}\|\boldsymbol{p}_c - \boldsymbol{p}_{c,g}\| & \text{if } \|\boldsymbol{p}_c - \boldsymbol{p}_{c,g}\| \geq d_{\mathcal{G}} \\ \frac{1}{2}k_{\mathcal{G},b}\|\boldsymbol{p}_c - \boldsymbol{p}_{c,g}\|^2 & \text{if } \|\boldsymbol{p}_c - \boldsymbol{p}_{c,g}\| < d_{\mathcal{G}} \end{cases} \quad (11)$$

where $\boldsymbol{p}_c$ is the current centroid of the microrobots' positions, $\boldsymbol{p}_{c,g}$ is the centroid position of the goal formation F_g, $d_{\mathcal{G}}$ is a distance threshold discriminating the cost function to consider, with $k_{\mathcal{G},a} > 0$ and $k_{\mathcal{G},b} > 0$, such that $k_{\mathcal{G},a} = d_{\mathcal{G}}k_{\mathcal{G},b}$ to guarantee continuity at the transition for $\|\boldsymbol{p}_c - \boldsymbol{p}_g\| = d_{\mathcal{G}}$. Finally, a suitable force that minimizes the cost function (11) is generated with a gradient descent approach as

$$\boldsymbol{f}_{\mathcal{G}} = \nabla\mathcal{J} = \begin{cases} k_{\mathcal{G},a}\dfrac{(\boldsymbol{p}_c - \boldsymbol{p}_g)}{\|\boldsymbol{p}_c - \boldsymbol{p}_g\|} & \text{if } \|\boldsymbol{p}_c - \boldsymbol{p}_g\| \geq d_{\mathcal{G}} \\ k_{\mathcal{G},b}(\boldsymbol{p}_c - \boldsymbol{p}_g) & \text{if } \|\boldsymbol{p}_c - \boldsymbol{p}_g\| < d_{\mathcal{G}}. \end{cases} \quad (12)$$

It is worth mentioning that this guidance steers the user towards the target formation *centroid*. The user will still need to adjust the orientation of the formation without aid since no torque feedback is provided by the haptic device.

C. Combination of Haptic and Shared Control Strategies

The force contributions described above can be directly provided to the microrobots through the BatMag system or to the human user through the Omega.6 haptic interface, depending on the condition at hand and the desired behavior.

The total force applied to each microrobot i is defined as

$$\boldsymbol{f}_{\mathcal{R},i} = \boldsymbol{f}_{\mathcal{T},i} + \boldsymbol{f}_{\mathcal{M},i} + \boldsymbol{f}_{\mathcal{D},i} + \boldsymbol{f}_{\mathcal{S},i}, \quad i = 1,2 \quad (13)$$

where: $\boldsymbol{f}_{\mathcal{T},i}$ is the force needed to teleoperate the robots, as defined in eq. (4); $\boldsymbol{f}_{\mathcal{M},i}$ is the force enforcing mutual avoidance between the robots, as defined in eq. (8); $\boldsymbol{f}_{\mathcal{D},i} = -k_{\mathcal{D}}\boldsymbol{v}_i$, with $k_{\mathcal{D}} > 0$, is a damping force, depending on the microrobot velocity $\boldsymbol{v}_i$, introduced to guarantee smoothness and stability during the system actuation; and $\boldsymbol{f}_{\mathcal{S},i}$ is the force due to the chosen shared control strategy, eventually embodying an assigned autonomous behaviour. As an example, if obstacle avoidance behaviour is handled autonomously, one has $\boldsymbol{f}_{\mathcal{S},i} = \boldsymbol{f}_{\mathcal{O},i}(\boldsymbol{p}_i, \boldsymbol{v}_i)$ (as will be detailed next in Sect. IV-B).

Eq. (13) effectively characterizes the nature of the shared control strategy: the total force $\boldsymbol{f}_{\mathcal{R},i}$ is generated by combining a user-generated contribution ($\boldsymbol{f}_{\mathcal{T},i}$) through the haptic interface, with autonomous contributions ($\boldsymbol{f}_{\mathcal{M},i}$, $\boldsymbol{f}_{\mathcal{S},i}$) derived from the system's control behaviors. This approach allows the user to command the primary motion direction of the microrobots, while the system autonomously adjusts the trajectory to incorporate additional tasks and ensure successful navigation. Forces $\boldsymbol{f}_{\mathcal{T},i}$, $\boldsymbol{f}_{\mathcal{D},i}$ and $\boldsymbol{f}_{\mathcal{M},i}$ are always present, while force $\boldsymbol{f}_{\mathcal{S},i}$ changes according to the considered condition (see Sec. IV-B). The total force $\boldsymbol{f}_{\mathcal{R},i}$ is applied to each microrobot i through the magnets of the BatMag control system.

On the other hand, the haptic feedback applied to the user through the haptic interface can be defined as

$$\boldsymbol{f}_{\mathcal{H}} = \boldsymbol{f}_{\mathcal{H}_{OA}} + \boldsymbol{f}_{\mathcal{H}_{GG}}, \quad (14)$$

where $\boldsymbol{f}_{\mathcal{H}_{OA}}$ is the force feedback providing information on the obstacle avoidance strategy, and $\boldsymbol{f}_{\mathcal{H}_{GG}}$ is the force providing information on the navigation goal guidance strategy.

The definition of the shared control strategy $\boldsymbol{f}_{\mathcal{S},i}$ and the haptic feedback $\boldsymbol{f}_{\mathcal{H}}$ are detailed in Sec. IV-B. Of course, other choices can be made according to the task at hand.

Finally, it is important to acknowledge that the use of potential-field-based input forces can expose the control strategy to issues such as local minima and oscillations, which are common drawbacks of potential-field methods. However, the shared control approach inherently mitigates these challenges, as the user's input allows the system to 'escape' from such conditions. When microrobots' trajectories encounter local minima, the user can quickly recognize the issue and adjust the direction of motion, thereby maintaining effective control. Similarly, any undesired oscillations are easily damped by the user grasping the end-effector of the haptic interface.

IV. EXPERIMENTAL EVALUATION

To assess the efficacy of the proposed haptic shared control system, we conducted a human subjects experiment. A video of the experiment is available as supplemental material and at https://youtu.be/QQhqrjMZGEU.

A. Experimental Setup

The setup is composed of the haptic-enabled teleoperation system described in Sec. II and shown in Fig. 1, which enables a human user to control the coordinated motion of a pair of microrobots while receiving suitable haptic feedback.

The environment in which the robots move is the full $22 \times 22 \times 22$ mm workspace of the BatMag system, populated by 7 virtual rectangular prisms (the obstacles), as shown in Figs. 5 and 6. Their positioning has been chosen to to recreate various challenging navigation tasks, i.e., by surrounding the goal configurations with varying number of obstacles.

B. Experimental Conditions

To ensure a precise mapping of the haptic device's motion to the microrobots' movement within the BatMag environment, parameters $l_{H,min}$, $l_{H,max}$, l_B, $\psi_{H,min}$, and $\psi_{H,max}$ were tailored to the Omega.6 and BatMag workspaces. Table I summarizes the parameter values used in our implementation[5]

We designed six control and rendering conditions, combining haptic and shared control strategies as discussed in Sec. III-C.

We considered three strategies for obstacle avoidance, which define $\boldsymbol{f}_{\mathcal{S},i}$ in eq. (13) and $\boldsymbol{f}_{\mathcal{H}_{OA}}$ in eq. (14):

---

[5]To implement the teleoperation contribution in the real experimental setup, we set $K_v = 0$ because the presence of silicon oil in the BatMag workspace naturally provides sufficient damping, stabilizing the microrobots' motion without the need for additional damping control. However, we kept a generic formulation of $\boldsymbol{f}_{\mathcal{T},i}$ in eq. (4) to accommodate other environments where an arbitrary damping term with $K_v \geq 0$ might be necessary.

TABLE I
CONTROL PARAMETERS USED IN OUR IMPLEMENTATION AND EXPERIMENTAL EVALUATION

Variable	Description	Value
K_p	Teleoperation proportional gain	1.2×10^{-2} N/m
K_v	Teleoperation derivative gain	0 N s/m
L_d	Desired formation length	4×10^{-3} m
α	Potential field constant	1.9×10^3 m^{-1}
$\rho_\mathcal{O}$	Obstacle avoidance gain	1×10^{-7} N m
$\rho_\mathcal{M}$	Mutual avoidance gain	5×10^{-7} N m
$k_{\mathcal{G},a}$	Guidance conical gain	2.25×10^{-1} N
$k_{\mathcal{G},b}$	Guidance paraboloidal gain	75 N/m
$d_\mathcal{G}$	Navigation guidance threshold	3×10^{-3} m
$k_\mathcal{D}$	Damping gain	1×10^{-3} N s/m
$k_\mathcal{H}$	Haptic obstacle avoidance gain	10^5

OA) *no obstacle avoidance aid*: no help in avoiding the obstacles, i.e., $f_{\mathcal{S},i} = \mathbf{0}$ and $f_{\mathcal{H}_{OA}} = \mathbf{0}$;

HOA) *haptic obstacle avoidance*: haptic cues pushing the user away from the obstacles, evaluating eq. (6) with respect to the reference robot motion ($p_{i,d}$, $v_{i,d}$) as retrieved by the haptic device, i.e.,

$$\begin{cases} f_{\mathcal{H}_{OA}} = k_\mathcal{H} \sum_{i=1}^{2} f_{\mathcal{O},i}(p_{i,d}, v_{i,d}) \\ f_{\mathcal{S},i} = \mathbf{0} \end{cases} \quad (15)$$

AOA) *autonomous obstacle avoidance*: the formation autonomously avoids the obstacles, evaluating eq. (6) with respect to the current robot state (p_i, v_i), i.e., $f_{\mathcal{S},i} = f_{\mathcal{O},i}(p_i, v_i)$, $i = 1, 2$ and $f_{\mathcal{H}_{OA}} = \mathbf{0}$.

We considered two strategies for navigation guidance towards the goal, which define $f_{\mathcal{H}_{GG}}$ in eq. (14):

GG) *no haptic goal guidance*: no help guiding the user towards the designated goal, i.e., $f_{\mathcal{H}_{GG}} = \mathbf{0}$;

HGG) *haptic goal guidance*: haptic cues guide the user towards the goal pose, i.e., $f_{\mathcal{H}_{GG}} = f_\mathcal{G}$.

The combination of the above obstacle avoidance and guidance strategies leads to six experimental conditions (as synthetized also in Table II): OA+GG (no obstacle avoidance, no haptic guidance), OA+HGG (no obstacle avoidance, haptic guidance), HOA+GG (haptic obstacle avoidance, no haptic guidance), HOA+HGG (haptic obstacle avoidance, haptic guidance), AOA+GG (autonomous obstacle avoidance, no haptic guidance), and AOA+HGG (autonomous obstacle avoidance, haptic guidance). The supplementary video shows the behavior of each of these conditions.

C. Experimental Task and Protocol

Participants were instructed to use the Omega.6 haptic interface to steer the microrobot formation across the remote environment, towards the predefined goal formation $F_g = \langle p_{c,g}, \phi_g, \theta_g, L_g \rangle$, as fast as possible and without colliding with the obstacles. We considered three goal formations (see Table III) to force the participants to move along different paths. Each path had the same length and level of difficulty with respect to the obstacles. The order of the experimental conditions was generated using a balanced Latin

TABLE II
THE COMBINATIONS OF OBSTACLE AVOIDANCE AND GUIDANCE STRATEGIES, DEFINING THE SIX EXPERIMENTAL CONDITIONS OF THE HUMAN SUBJECTS EXPERIMENT. OBSTACLE AVOIDANCE STRATEGIES: ABSENT (OA), HAPTIC (HOA), AUTONOMOUS (AOA). GOAL GUIDANCE STRATEGIES: ABSENT (GG), HAPTIC (HGG)

		Obstacle avoidance		
		no	haptic	autonomous
Goal guidance	no	OA+GG	HOA+GG	AOA+GG
	haptic	OA+HGG	HOA+HGG	AOA+HGG

TABLE III
THE THREE GOAL CONFIGURATIONS FOR THE FORMATION USED IN THE EXPERIMENT, WITH THE FORMATION CENTROID POSITION ($p_{c,g}$ [mm]), ORIENTATIONS (ϕ_g, θ_g [°]) AND MICROROBOTS DISTANCE (L_g [mm]), EXPRESSED IN THE BATMAG REFERENCE FRAME $\mathcal{F}_B$

Goal	Configuration ($p_{c,g}, \phi_g, \theta_g, L_g$) in $\mathcal{F}_B$
1	$(0.0, 6.0, 9.0, 0, -90, 4.0)$
2	$(-3.0, -3.0, 4.5, 30, -90, 4.0)$
3	$(5.0, 2.0, 3.0, 0, -45, 4.0)$

square, so as to minimize learning effects across participants. Each participant carried the task exactly six times, once per experimental condition, and twice per goal. The order in which the goals were presented did not change across subjects. The task was considered completed when the user positioned the two microrobots within 750 μm of the corresponding targets for more than 1 s, similarly to [34].

As shown in Figs. 1 and 5, participants saw the remote environment through top and side camera views of the BatMag system. The virtual obstacles were superposed on the images, along with the robots goal, reference, and current positions. [6]

D. Participants

18 participants took part in the experiment (3 women, 15 men, age 21-37 y.o., mean self-assessed experience with haptics 3.2/10, mean self-assessed experience with electromagnetic systems 4.6/10). Participants were recruited at the University of Twente, mostly among students, postdocs, technicians, and secretaries from science, technology, engineering and mathematics (STEM) disciplines. Before starting the experiment, participants tested the haptic device and teleoperation control in a virtual environment (similar to Fig. 6), where they could get familiar with the teleoperation control apparatus and navigation task with no external support, i.e., as in condition OA+GG. The experiment lasted approximately 45 minutes, including the initial training.

E. Evaluation Metrics

To evaluate the effectiveness of the six conditions under test, we considered the average navigation time, the number

---

[6]In order to appropriately investigate the effectiveness of the haptic feedback in the designed control strategies and to maintain the complexity of the experimental study tractable, here we deliberately did not leverage the augmented visual feedback information provided by *digital twin* system described in Sect. II-D. A multimodal analysis combining visual and haptic cues is not part of this study and will be object of future works.

of collisions against the obstacles, and the positioning error with respect to the assigned goal. Moreover, at the end of the experiment, subjects were asked to fill out a questionnaire evaluating the perceived effectiveness of each condition, from 0 (very ineffective) to 10 (very effective). We also asked them to choose which condition was perceived as the most intuitive and effective with respect to the navigation task. Finally, we encouraged participants to leave open comments about the teleoperation system, control algorithms, and tasks.

F. Results

To compare the different metrics, we ran two-way repeated-measures ANOVA tests (significance level a = 0.05). ANOVA is a popular collection of statistical models and estimation tools used to analyze *differences* among group means in a sample. The obstacle avoidance (~~OA~~ vs. HOA vs. AOA) and guidance (~~GG~~ vs. HGG) techniques were the within-subject factors. A Greenhouse-Geisser correction was used when the assumption of sphericity was violated. Sphericity was assumed for variables with only two levels of repeated measures (the guidance technique). Results of post hoc analysis with Bonferroni adjustments are reported in Table IV and Figs. 7-8 (only significant p values are shown).

Fig. 7a shows the task completion time. All data passed the Mauchly's Test of Sphericity. The two-way repeated-measure ANOVA revealed a statistically significant change for this metric across obstacle avoidance ($F_{(2,34)} = 5.487$, $p = 0.009$) and guidance ($F_{(1,17)} = 6084.897$, $p = 0.038$) techniques.

Fig. 7b shows the number of collisions with the obstacles. Mauchly's Test of Sphericity indicated that the assumption of sphericity had been violated for the avoidance variable ($\chi^2(2) = 26.145$, $p < 0.001$) and the avoidance*guidance variables interaction ($\chi^2(2) = 21.998$, $p < 0.001$). The two-way repeated-measure ANOVA revealed a statistically significant change for this metric across obstacle avoidance techniques ($F_{(1.108,18.838)} = 16.345$, $p = 0.001$).

Fig. 7c shows the positioning error at the end of the task, calculated as the average positioning error of the two microrobots. All data passed the Mauchly's Test of Sphericity test. The two-way repeated-measure ANOVA revealed a statistically significant two-way interaction between control and feedback variables ($F_{(2, 34)} = 1174.153$, $p < 0.001$). When a statistically significant interaction between variables is found, we need to analyze the simple main effects. Interpreting the simple main effects for the obstacle avoidance variable, we found a statistically significant difference (~~OA~~-~~GG~~ vs. HOA-~~GG~~ vs. AOA-~~GG~~: $F_{(2,34)} = 15.157$, $p < 0.001$; ~~OA~~-HGG vs. HOA-HGG vs. AOA-HGG: $F_{(1.417,24.092)} = 2240.304$, $p < 0.001$). Interpreting the simple main effects for the guidance variable, we found a statistically significant difference (~~OA~~-~~GG~~ vs. ~~OA~~-HGG, $t(17)=64.750$, $p < 0.001$; HOA-~~GG~~ vs. HOA-HGG, $t(17)=4.709$, $p < 0.001$; AOA-~~GG~~ vs. AOA-HGG, $t(17)=70.741$, $p < 0.001$).

Fig. 8 shows the perceived effectiveness, as rated by the users at the end of the experiment (10 being the best). Mauchly's Test of Sphericity indicated that the assumption of sphericity had been violated for the avoidance variable ($\chi^2(2) = 22.360$, $p < 0.001$) and the avoidance*guidance variables interaction ($\chi^2(2) = 16.674$, $p < 0.001$). The

TABLE IV
HUMAN PARTICIPANT STUDY

Conditions	Obstacle avoidance
	~~OA~~ (no obstacle avoidance), HOA (haptic obstacle avoid.), AOA (autonomous obstacle avoid.)
	Navigation guidance
	~~GG~~ (no guidance), HGG (haptic guidance)

Statistical analysis (only significant p values are shown, in **bold** the best condition)

Completion time
    Main effect of obstacle avoidance
    HOA vs. **AOA** $p = 0.029$

Number of collisions
    Main effect of obstacle avoidance
    ~~OA~~ vs. **HOA** $p = 0.003$ ~~OA~~ vs. **AOA** $p = 0.029$
    HOA vs. **AOA** $p = 0.044$

Positioning error
  Simple main effect of obstacle avoidance
    ~~OA~~+~~GG~~ vs. **HOA+~~GG~~** $p < 0.001$ **HOA+~~GG~~** vs. AOA+~~GG~~ $p = 0.001$
    ~~OA~~+HGG vs. HOA+HGG $p < 0.001$ HOA+HGG vs. **AOA+HGG** $p < 0.001$
  Simple main effect of guidance
    ~~OA~~-~~GG~~ vs. ~~OA~~-HGG $p < 0.001$ HOA-~~GG~~ vs. **HOA-HGG** $p < 0.001$
    AOA-~~GG~~ vs. **AOA-HGG** $p < 0.001$

Perceived effectiveness
    Main effect of obstacle avoidance
    ~~OA~~ vs. **HOA** $p < 0.001$ **HOA** vs. AOA $p = 0.002$

Most effective experimental condition as chosen by subjects
One subject out of eighteen chose HOA+~~GG~~, four chose AOA+~~GG~~, one chose ~~OA~~+HGG, six chose HOA+HGG, and six chose AOA+HGG.

two-way repeated-measure ANOVA revealed a statistically significant change for this metric across obstacle avoidance ($F_{(1,19.398)} = 21.520$, $p < 0.001$) and guidance ($F_{(1,17)} = 71.261$, $p < 0.001$) techniques. Finally, participants were asked to choose which condition they preferred overall: one participant chose HOA+~~GG~~, four chose AOA+~~GG~~, one chose ~~OA~~+HGG, six chose HOA+HGG, and six chose AOA+HGG.

G. Discussion

Our results demonstrably show that assisting in avoiding obstacles guarantees safer performance and nullifies the occurrence of collisions of the microrobots, regardless if the assistance is autonomous (AOA) or delivered through a haptic repulsive force (HOA). Additionally, the autonomous obstacle avoidance (AOA) reduces the overall travel time by 30% compared to no obstacle avoidance (~~OA~~) and haptic obstacle avoidance (HOA). On the other hand, guidance provided through haptic feedback (HGG) is preferred by users, as they feel "more in control" and "aware of what is happening".

We also observe that a combination of haptic obstacle avoidance and goal guidance (HOA+HGG) resulted in undesired collisions. This is in agreement with previous studies, proving that providing different information through the same sensory channel could be ambiguous and degrade performances during
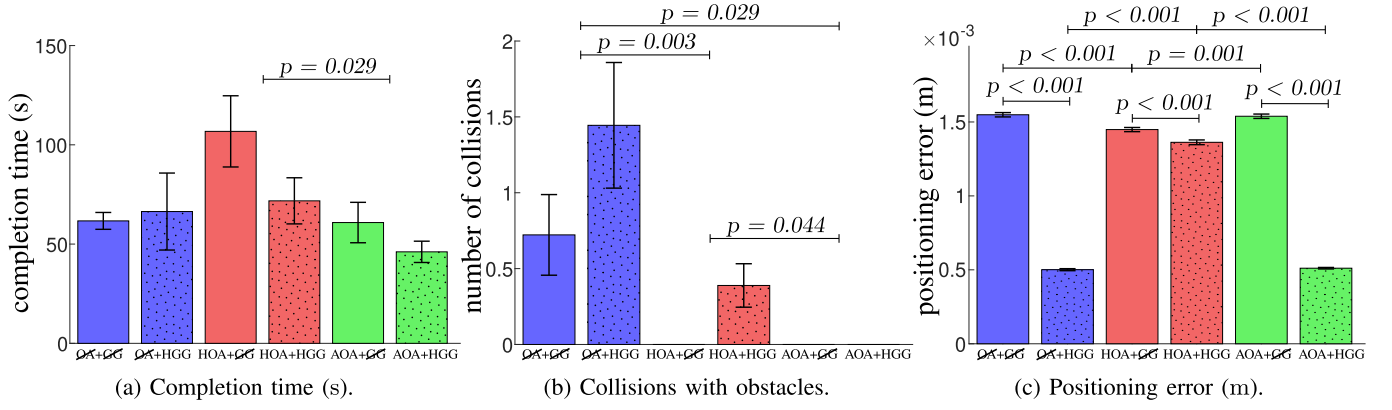
Fig. 7. Human-subjects navigation experiment: objective metrics. Mean and standard error of (a) completion time, (b) collisions with the obstacles, and (c) positioning error for conditions OA+GG, OA+HGG, HOA+GG, HOA+HGG, AOA+GG, and AOA+HGG (see Table IV).
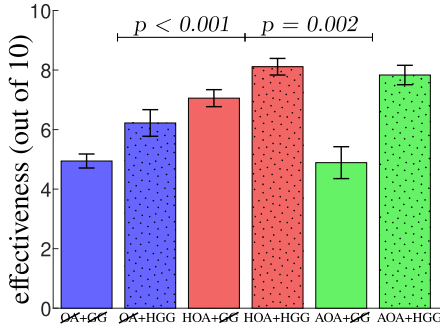

Fig. 8. Human-subjects navigation experiment: subjective metrics. Mean and standard error of the perceived effectiveness for conditions OA+GG, OA+HGG, HOA+GG, HOA+HGG, AOA+GG, and AOA+HGG (see Table IV).

haptic teleoperation [16]. In fact, the user is unsure if the force felt is due to guidance or obstacle avoidance. Nevertheless, the condition providing both haptic obstacle avoidance and guidance (HOA+HGG) was the most preferred by users. Finally, providing guidance assistance (HGG) improved the positioning accuracy at the end of the task by 65%, with respect to not providing guidance assistance (GG).

V. GENERALIZATION TO N-ROBOTS FORMATION CONTROL

The presented shared control techniques have been deployed and experimentally evaluated to control a *pair* of microrobots. In this respect, the independent control of the two agents would have also been certainly possible using two separate devices, each controlling one robot. However, such approach would have likely led to a higher mental load for the users, and it is clearly not scalable to a higher number of robots. Instead, our primary motivation in developing these control strategies has been to establish a solution for the intuitive control of multiple microrobots.

In fact, although experimentally we show the formation control of only two microrobots, due to the limitations of the actuation system, the proposed control strategies can be scaled to $N > 2$ microrobots. In this Section, we formalize the generalization of the shared control strategy for formations of N microrobots. The resulting control scheme will generate the necessary force inputs for each microrobot in the formation to accomplish the assigned tasks. Of course, the actual successful navigation is contingent upon the electromagnetic actuation system's ability to independently control the N microrobots.

Formally, we can generalize eq. (3) so as to consider a desired formation that equally spaces the N microrobots over a circular area of radius $L_d/2$, i.e., the position of the i-th microrobot in the base reference frame $\mathcal{F}_B$ is given by

$$\boldsymbol{p}_{i,d} = \boldsymbol{p}_{c,d} + {}^{B}\boldsymbol{R}_F(\phi_d, \theta_d) \, {}^{F}\boldsymbol{p}_i, \quad i = 1, \ldots, N \quad (16)$$

with

$$ {}^{F}\boldsymbol{p}_i = \frac{L_d}{2}\left[\cos(\tfrac{2\pi i}{N} + \alpha) \, \sin(\tfrac{2\pi i}{N} + \alpha) \, 0\right]^{T}, \quad (17)$$

where α is an optional angular offset. Examples of this generalized formation are sketched in Figs. 9a-9b, where we show illustrative cases of 3- and 4-microrobots formation, having $\alpha = 0$ and $\alpha = \pi/4$, respectively. For each i-th microrobot, the desired positions (16) are used as reference for the control law (4), generating the corresponding contribution $\boldsymbol{f}_{\mathcal{T},i}$. Furthermore, obstacle avoidance behaviors unalteredly apply through eqs. (5)-(6), while the mutual avoidance contribution from the potential function (7) generalizes as

$$g_{\mathcal{M}}(\boldsymbol{p}_i) = \frac{1}{2}\sum_{j=1}^{N} e^{-\alpha\|\boldsymbol{p}_i - \boldsymbol{p}_j\|_2}, \quad i = 1, \ldots, N \quad i \neq j. \quad (18)$$

Finally, navigation guidance haptic contributions also apply unalteredly through eqs. (11)-(12), since they depend on the formation centroid $\boldsymbol{p}_{c,d}$ only. A demonstration of 3- and 4-microrobots formations, navigating the virtual BatMag environment among the obstacles, is available as supplemental material and at https://youtu.be/QQhqrjMZGEU.

VI. USE CASE SCENARIO: NAVIGATION IN A SIMULATED ENDOVASCULAR ENVIRONMENT

The presented control architecture is adaptable to different application fields that can benefit from the deployment of multiple coordinated microrobots. One significant area of application is in clinical settings [5], where the use of microrobots can enhance the precision and effectiveness of minimally invasive procedures. Furthermore, shared control strategies are particularly beneficial in these contexts as they combine the clinician's expertise with the system's automation and accuracy capabilities, enabling more precise and controlled manipulation in complex and delicate environments, such as those encountered in medical interventions.
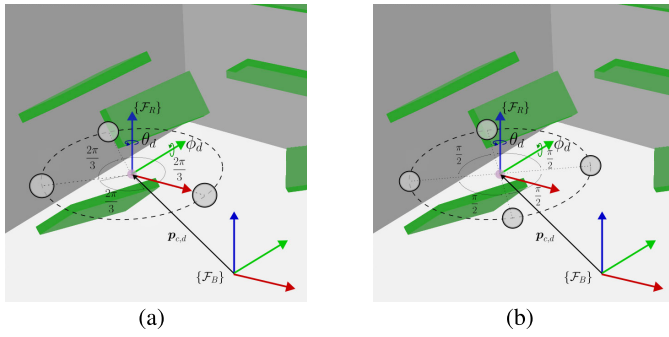
Fig. 9. (a) 3-microrobot formation, with microrobots equally spaced over a circular area of radius $L_d/2$ and no angular offset ($\alpha = 0$); (b) 4-microrobot formation, with microrobots equally spaced over a circular area of radius $L_d/2$ with an angular offset of $\alpha = \pi/4$. The desired positions for the microrobots are determined by (16).
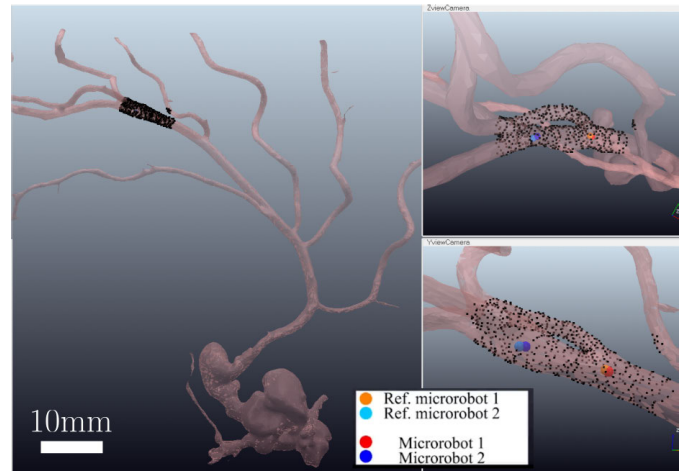

Fig. 10. The 3D endovascular workspace recreated in the simulation environment from available CT scans. Black dots represent the closest vertices of the 3D endovascular model to the microrobots' formation.

To illustrate this potential, we designed a use case scenario that employs the proposed haptic shared control methodologies to enable endovascular navigation of microrobots within a virtual environment simulating the complex and intricate structure of blood vessels. The virtual endovascular navigation was implemented using the CoppeliaSim simulation software. A 3D model of the considered vascular system was reconstructed from real CT scans of a human brain affected by a fusiform aneurysm, as shown in Fig. 10. The modeling process utilized the 3DSlicer open-source software[7] to process the CT images, employing semi-autonomous segmentation and labeling tools to highlight the vascular structures across the three scan axes.

The motion of a pair of microrobots was commanded in a shared control fashion. To manage the complexity and larger scale of the environment, the microrobots' teleoperation was achieved by integrating velocity-based reference commands provided by the user through the haptic interface, i.e.,

$$\boldsymbol{p}_{i,d} = \boldsymbol{p}_{i,0} + \int \boldsymbol{v}_{c,d}(t)dt, \quad i = 1, 2$$
$$\begin{pmatrix} \phi_d \\ \theta_d \end{pmatrix} = \begin{pmatrix} \phi_0 \\ \theta_0 \end{pmatrix} + \int \dot{\boldsymbol{q}}_{\{4-6\}}(t)dt. \tag{19}$$

A clutch-based mechanism, implemented via keyboard input, handles the kinematic dissimilarity between the haptic device and the endovascular workspace: this allows the user to disable teleoperation when the joint limits of the haptic device are reached, reconfigure the device handle to a more suitable configuration, and then restore teleoperation, enabling the exploration of target workspaces of arbitrary size.

To implement obstacle avoidance, the vertex positions of the 3D model of the vascular system are extracted in the simulation environment. The closest $N_\mathcal{O}$ vertices to the microrobots (shown as black dots in Fig. 10), within a predefined distance threshold d_O, are then selected as point obstacles $\boldsymbol{p}_{\mathcal{O},j}$ to define the repulsive potential field (5). This setup allows the system to provide autonomous and haptic obstacle avoidance behaviors as described by eqs. (6)-(15). A video demonstrating the microrobots' navigation within this virtual endovascular environment is available as supplemental material and at https://youtu.be/QQhqrjMZGEU.

[7]https://www.slicer.org

VII. FUTURE PERSPECTIVES AND APPLICABILITY

Besides the clinical application on endovascular navigation, illustrated in the previous Section, the presented architecture can be also adapted to other fields, that would benefit of the deployment of multiple microrobot systems. As an example:

- *environmental remediation*: multiple microrobots (e.g., magnetic Janus particles, coated according to the polluting substance to be cleaned) are deployed in a polluted aqueous environment; shared control techniques can enable a single user to control, e.g., the centroid of the swarm, while size and shape are adapted automatically according to the location of the polluted substance;

- *micromanipulation and bioengineering*: pairs of microrobots can grasp objects at the microscale, demonstrating assembly of micromachines (e.g., using components fabricated by stereolithography) and of cell/tissue engineering constructs (e.g., using cells and biomaterials); shared control techniques can enable a single user to control the centroid of the two robots, while the grasping action is controlled autonomously according to the task at hand.

Moreover, additional shared control strategies can be implemented on top of the obstacle avoidance and navigation techniques presented in this work, according to the needs of the application at hand. For example, we have recently demonstrated autonomous object grasping and micromanipulation with the considered BatMag electromagnetic system [1]; in this context, the proposed haptic shared control methodologies can enable a human user to control such a process, including the specificities of the task in the design of the shared control (e.g., controlling directly the motion of the grasped object, guidance for precise positioning and assembly, optimized grasping poses, stable grasping during delivery).

Finally, the availability of the *digital twin* system can be leveraged to introduce additional sensory feedback and physically interact with the user, while further enhancing its perception of the environment and understanding of the task. This revised technological paradigm (also referred to as *phygital twin*, from the merging of *physical* and *digital* [47])

can stand as a valuable assistive tool for the accomplishment of complex tasks, as we have shown at the macro-scale [16], [48].

In future work, we plan to integrate haptic devices with 6 active DoFs to include torque feedback for formation orientation guidance. We also aim to address real-world constraints in the shared control strategy, such as microrobot self-occlusions and workspace limitations, while considering additional metrics like NASA TLX and SUS. Finally, we will investigate switching methods to, e.g., automatically adjust the level of autonomy in the control, as we have already recently started to study [49].
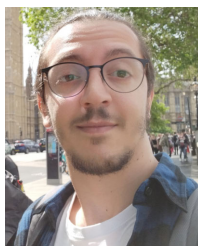
VIII. CONCLUSION

This work presents a haptic-enabled shared control teleoperation system of a pair of electromagnetic microrobots. The system aims at combining the robustness and repeatability of autonomous control with the dexterity and experience of a human operator. As a representative example, we consider safe navigation in an environment cluttered with obstacles. A human user steers the two microrobots across the environment, avoiding collisions with obstacles thanks to the aid of the presented shared control strategies.

We conducted a user study on the BatMag electromagnetic system to evaluate the effectiveness of various haptic shared control strategies for safe navigation. Results showed that autonomous obstacle avoidance minimized collisions and reduced travel time, while haptic guidance improved task accuracy. However, combining haptic obstacle avoidance with goal guidance sometimes led to safety compromises and unwanted collisions. Additionally, we showed the scalability of the proposed control to formations of N microrobots, extending its applicability beyond the initial two-microrobot setup. Leveraging a simulation environment, we showcased its potential for a more complex endovascular navigation use case, emphasizing its suitability for intricate medical procedures like targeted drug delivery and aneurysm treatment.

REFERENCES

[1] F. N. Piñan Basualdo and S. Misra, "Collaborative magnetic agents for 3D microrobotic grasping," *Adv. Intell. Syst.*, vol. 5, no. 12, Dec. 2023, Art. no. 2300365.

[2] S. Shivalkar et al., "Autonomous magnetic microbots for environmental remediation developed by organic waste derived carbon dots," *J. Environ. Manage.*, vol. 297, Nov. 2021, Art. no. 113322.

[3] C. Wang, A. Mzyk, R. Schirhagl, S. Misra, and V. K. Venkiteswaran, "Biocompatible film-coating of magnetic soft robots for mucoadhesive locomotion," *Adv. Mater. Technol.*, vol. 8, no. 12, Jun. 2023, Art. no. 2201813.

[4] B. J. Nelson and S. Pané, "Delivering drugs with microrobots," *Science*, vol. 382, no. 6675, pp. 1120–1122, Dec. 2023.

[5] V. Iacovacci, E. Diller, D. Ahmed, and A. Menciassi, "Medical microrobots," *Annu. Rev. Biomed. Eng.*, vol. 26, no. 1, pp. 561–591, Jul. 2024.

[6] A. Bolopion and S. Régnier, "A review of haptic feedback teleoperation systems for micromanipulation and microassembly," *IEEE Trans. Autom. Sci. Eng.*, vol. 10, no. 3, pp. 496–502, Jul. 2013.

[7] C. Pacchierotti, S. Scheggi, D. Prattichizzo, and S. Misra, "Haptic feedback for microrobotics applications: A review," *Frontiers Robot. AI*, vol. 3, p. 53, Aug. 2016.

[8] H. Wang et al., "Data-driven parallel adaptive control for magnetic helical microrobots with derivative structure in uncertain environments," *IEEE Trans. Syst., Man, Cybern., Syst.*, vol. 54, no. 7, pp. 4139–4150, Jul. 2024.

[9] S. Zhong et al., "Spatial constraint-based navigation and emergency replanning adaptive control for magnetic helical microrobots in dynamic environments," *IEEE Trans. Autom. Sci. Eng.*, early access, Dec. 20, 2023, doi: 10.1109/TASE.2023.3339637.

[10] C. Huang, T. Xu, and X. Wu, "Leader-follower formation control of magnetically actuated millirobots for automatic navigation," *IEEE/ASME Trans. Mechtron.*, vol. 29, no. 2, pp. 1272–1282, Apr. 2024.

[11] A. Franchi, C. Secchi, M. Ryll, H. H. Bulthoff, and P. R. Giordano, "Shared control: Balancing autonomy and human assistance with a group of quadrotor UAVs," *IEEE Robot. Autom. Mag.*, vol. 19, no. 3, pp. 57–68, Sep. 2012.

[12] C. Pacchierotti and D. Prattichizzo, "Cutaneous/tactile haptic feedback in robotic teleoperation: Motivation, survey, and perspectives," *IEEE Trans. Robot.*, vol. 40, pp. 978–998, 2024.

[13] M. Niccolini, V. Castelli, C. Diversi, B. Kang, F. Mussa, and E. Sinibaldi, "Development and preliminary assessment of a robotic platform for neuroendoscopy based on a lightweight robot," *Int. J. Med. Robot. Comput. Assist. Surgery*, vol. 12, no. 1, pp. 4–17, Mar. 2016.

[14] M. Marcano, S. Díaz, J. Pérez, and E. Irigoyen, "A review of shared control for automated vehicles: Theory and applications," *IEEE Trans. Hum.-Mach. Syst.*, vol. 50, no. 6, pp. 475–491, Dec. 2020.

[15] A. Weiss, A.-K. Wortmeier, and B. Kubicek, "Cobots in Industry 4.0: A roadmap for future practice studies on human–robot collaboration," *IEEE Trans. Hum.-Mach. Syst.*, vol. 51, no. 4, pp. 335–345, Aug. 2021.

[16] M. Ferro, C. Pacchierotti, S. Rossi, and M. Vendittelli, "Deconstructing haptic feedback information in robot-assisted needle insertion in soft tissues," *IEEE Trans. Haptics*, vol. 16, no. 4, pp. 536–542, Oct. 2023.

[17] A. Mohebbi, "Human–robot interaction in rehabilitation and assistance: A review," *Current Robot. Rep.*, vol. 1, no. 3, pp. 131–144, Sep. 2020.

[18] F. Morbidi et al., "Assistive robotic technologies for next-generation smart wheelchairs: Codesign and modularity to improve users' quality of life," *IEEE Robot. Autom. Mag.*, vol. 30, no. 1, pp. 24–35, Mar. 2023.

[19] U. Bozuyuk, P. Wrede, E. Yildiz, and M. Sitti, "Roadmap for clinical translation of mobile microrobotics," *Adv. Mater.*, vol. 36, no. 23, Jun. 2024, Art. no. 2311462.

[20] M. Selvaggio, F. Abi-Farraj, C. Pacchierotti, P. R. Giordano, and B. Siciliano, "Haptic-based shared-control methods for a dual-arm system," *IEEE Robot. Autom. Lett.*, vol. 3, no. 4, pp. 4249–4256, Oct. 2018.

[21] M. Selvaggio, J. Cacace, C. Pacchierotti, F. Ruggiero, and P. R. Giordano, "A shared-control teleoperation architecture for non-prehensile object transportation," *IEEE Trans. Robot.*, vol. 38, no. 1, pp. 569–583, Feb. 2022.

[22] K. T. Ly, M. Poozhiyil, H. Pandya, G. Neumann, and A. Kucukyilmaz, "Intent-aware predictive haptic guidance and its application to shared control teleoperation," in *Proc. 30th IEEE Int. Conf. Robot Human Interact. Commun. (RO-MAN)*, Aug. 2021, pp. 565–572.

[23] M. Abayazid, C. Pacchierotti, P. Moreira, R. Alterovitz, D. Prattichizzo, and S. Misra, "Experimental evaluation of co-manipulated ultrasound-guided flexible needle steering," *Int. J. Med. Robot. Comput. Assist. Surgery*, vol. 12, no. 2, pp. 219–230, Jun. 2016.

[24] M. Aggravi, D. A. L. Estima, A. Krupa, S. Misra, and C. Pacchierotti, "Haptic teleoperation of flexible needles combining 3D ultrasound guidance and needle tip force feedback," *IEEE Robot. Autom. Lett.*, vol. 6, no. 3, pp. 4859–4866, Jul. 2021.

[25] R. Rahal, A. M. Ghalamzan-E, F. Abi-Farraj, C. Pacchierotti, and P. R. Giordano, "Haptic-guided grasping to minimise torque effort during robotic telemanipulation," *Auto. Robots*, vol. 47, no. 4, pp. 405–423, Apr. 2023.

[26] D. H. Lee, S. S. Lee, C. K. Ahn, P. Shi, and C.-C. Lim, "Finite distribution estimation-based dynamic window approach to reliable obstacle avoidance of mobile robot," *IEEE Trans. Ind. Electron.*, vol. 68, no. 10, pp. 9998–10006, Oct. 2021.

[27] M. Aggravi, C. Pacchierotti, and P. R. Giordano, "Connectivity-maintenance teleoperation of a UAV fleet with wearable haptic feedback," *IEEE Trans. Autom. Sci. Eng.*, vol. 18, no. 3, pp. 1243–1262, Jul. 2021.

[28] J. Storms, K. Chen, and D. Tilbury, "A shared control method for obstacle avoidance with mobile robots and its interaction with communication delay," *Int. J. Robot. Res.*, vol. 36, nos. 5–7, pp. 820–839, Jun. 2017.

[29] A. Gottardi, S. Tortora, E. Tosello, and E. Menegatti, "Shared control in robot teleoperation with improved potential fields," *IEEE Trans. Hum.-Mach. Syst.*, vol. 52, no. 3, pp. 410–422, Jun. 2022.

[30] W. Yuan and Z. Li, "Brain teleoperation control of a nonholonomic mobile robot using quadrupole potential function," *IEEE Trans. Cognit. Develop. Syst.*, vol. 11, no. 4, pp. 527–538, Dec. 2019.

[31] J. Luo, Z. Lin, Y. Li, and C. Yang, "A teleoperation framework for mobile robots based on shared control," *IEEE Robot. Autom. Lett.*, vol. 5, no. 2, pp. 377–384, Apr. 2020.

[32] L. Yang, J. Yu, S. Yang, B. Wang, B. J. Nelson, and L. Zhang, "A survey on swarm microrobotics," *IEEE Trans. Robot.*, vol. 38, no. 3, pp. 1531–1551, Jun. 2022.

[33] G. Lucarini et al., "Navigation of magnetic microrobots with different user interaction levels," *IEEE Trans. Autom. Sci. Eng.*, vol. 11, no. 3, pp. 818–827, Jul. 2014.

[34] C. Pacchierotti, V. Magdanz, M. Medina-Sánchez, O. G. Schmidt, D. Prattichizzo, and S. Misra, "Intuitive control of self-propelled microjets with haptic feedback," *J. Micro-Bio Robot.*, vol. 10, nos. 1–4, pp. 37–53, Oct. 2015.

[35] X. Zhang, H. Kim, and M. J. Kim, "Design, implementation, and analysis of a 3-D magnetic tweezer system with high magnetic field gradient," *IEEE Trans. Instrum. Meas.*, vol. 68, no. 3, pp. 680–687, Mar. 2019.

[36] E. Al Khatib, X. Zhang, M. J. Kim, and Y. Hurmuzlu, "Teleoperation control scheme for magnetically actuated microrobots with haptic guidance," *J. Micro-Bio Robot.*, vol. 16, no. 2, pp. 161–171, Dec. 2020.

[37] J. Lee, X. Zhang, C. H. Park, and M. J. Kim, "Real-time teleoperation of magnetic force-driven microrobots with 3D haptic force feedback for micro-navigation and micro-transportation," *IEEE Robot. Autom. Lett.*, vol. 6, no. 2, pp. 1769–1776, Apr. 2021.

[38] C. Pacchierotti et al., "Steering and control of miniaturized untethered soft magnetic grippers with haptic assistance," *IEEE Trans. Autom. Sci. Eng.*, vol. 15, no. 1, pp. 290–306, Jan. 2018.

[39] E. Diller, J. Giltinan, and M. Sitti, "Independent control of multiple magnetic microrobots in three dimensions," *Int. J. Robot. Res.*, vol. 32, no. 5, pp. 614–631, Apr. 2013.

[40] S. Chowdhury, W. Jing, and D. J. Cappelleri, "Controlling multiple microrobots: Recent progress and future challenges," *J. Micro-Bio Robot.*, vol. 10, nos. 1–4, pp. 1–11, Oct. 2015.

[41] E. Gerena, F. Legendre, A. Molawade, Y. Vitry, S. Régnier, and S. Haliyo, "Tele–robotic platform for dexterous optical single-cell manipulation," *Micromachines*, vol. 10, no. 10, p. 677, Oct. 2019.

[42] F. N. P. Basualdo, A. Bolopion, M. Gauthier, and P. Lambert, "A microrobotic platform actuated by thermocapillary flows for manipulation at the air-water interface," *Sci. Robot.*, vol. 6, no. 52, Mar. 2021, Art. no. eabd3557.

[43] T. Kawaguchi, Y. Inoue, M. Ikeuchi, and K. Ikuta, "Independent actuation and master-slave control of multiple micro magnetic actuators," in *Proc. IEEE Micro Electro Mech. Syst. (MEMS)*, Jan. 2018, pp. 190–193.

[44] B. Ahmad, M. Gauthier, G. J. Laurent, and A. Bolopion, "Mobile microrobots for in vitro biomedical applications: A survey," *IEEE Trans. Robot.*, vol. 38, no. 1, pp. 646–663, Feb. 2022.

[45] F. Ongaro, S. Pane, S. Scheggi, and S. Misra, "Design of an electromagnetic setup for independent three-dimensional control of pairs of identical and nonidentical microrobots," *IEEE Trans. Robot.*, vol. 35, no. 1, pp. 174–183, Feb. 2019.

[46] F. N. P. Basualdo, A. Bolopion, M. Gauthier, and P. Lambert, "Solving the non-linear motion in a micromanipulation system powered by thermocapillary flows," *IEEE Robot. Autom. Lett.*, vol. 8, no. 8, pp. 4785–4790, Aug. 2023.

[47] G. Barresi, C. Pacchierotti, M. Laffranchi, and L. De Michieli, "Beyond digital twins: Phygital twins for neuroergonomics in human–robot interaction," *Frontiers Neurorobotics*, vol. 16, Jun. 2022, Art. no. 913605.

[48] M. Ferro, C. Gaz, M. Anzidei, and M. Vendittelli, "Online needle-tissue interaction model identification for force feedback enhancement in robot-assisted interventional procedures," *IEEE Trans. Med. Robot. Bionics*, vol. 3, no. 4, pp. 936–947, Nov. 2021.

[49] E. Turco, C. Castellani, V. Bo, C. Pacchierotti, D. Prattichizzo, and T. L. Baldi, "Reducing cognitive load in teleoperating swarms of robots through a data-driven shared control approach," in *Proc. IEEE/RSJ Int. Conf. Intell. Robots Syst. (IROS)*, Oct. 2024, pp. 1–9.

Franco N. Piñan Basualdo received the master's degree in mechanical engineering from Instituto Balseiro, Universidad Nacional de Cuyo, San Carlos de Bariloche, Argentina, in 2018, and the Ph.D. degree in engineering sciences and technology from Université Libre de Bruxelles, Brussels, Belgium, and the Ph.D. degree in automation from Université Bourgogne Franche-Comté, Besançon, France, in the framework of a double degree program, in 2022. He was a Visiting Researcher with the Physical Intelligence Department, Max Planck Institute for Intelligent Systems, Stuttgart, Germany, in 2021. He is currently a Post-Doctoral Fellow with the Surgical Robotics Laboratory, University of Twente, Enschede, The Netherlands. Throughout his academic career, he has contributed to small-scale robotics by developing non-contact actuation mechanisms and their associated control. His research interests include microrobotics, soft robotics, swarm robotics, microfluidics, and applied physics.

Paolo Robuffo Giordano (Senior Member, IEEE) received the M.Sc. degree in computer science engineering and the Ph.D. degree in systems engineering from the University of Rome "La Sapienza" in 2001 and 2008, respectively. In 2007 and 2008, he spent one year as a Post-Doctoral Researcher with the Institute of Robotics and Mechatronics, German Aerospace Center (DLR), and from 2008 to 2012, he was a Senior Research Scientist with the Max Planck Institute for Biological Cybernetics, Tübingen, Germany. He is currently the Senior CNRS Researcher Head of the Rainbow Group, IRISA, and Inria, Rennes, France. He received the 2018 IEEE Robotics and Automation Letters Best Paper Award and he is an Editor of IEEE TRANSACTIONS ON ROBOTICS.

Sarthak Misra (Senior Member, IEEE) received the master's degree in mechanical engineering from McGill University, Montreal, QC, Canada, in 2001, and the Ph.D. degree in mechanical engineering from Johns Hopkins University, Baltimore, MD, USA, in 2009. He is currently a Professor with the Department of Biomechanical Engineering, University of Twente, Enschede, The Netherlands, and also with the Department of Biomedical Engineering, University of Groningen and University Medical Center Groningen, Groningen, The Netherlands. Prior to commencing his studies with Johns Hopkins University, he was a Dynamics and Controls Analyst with the International Space Station Program for three years. His research interests include surgical robotics and medical microrobotics. He was a recipient of the European Research Council Starting and Proof-of-Concept Grants and the Netherlands Organization for Scientific Research VENI and VIDI Award. He is the Co-Chair of the Robotics and Automation Society Technical Committee on Surgical Robotics and the International Federation of Automatic Control Technical Committee on Biological and Medical Systems.

Marco Ferro received the Ph.D. degree in automation, bioengineering, and operational research from the Department of Computer, Control, and Management Engineering (DIAG), Sapienza University of Rome, Italy, in 2019. He has been a Post-Doctoral Researcher with CNRS-IRISA, Rennes, France, since 2022. He was previously a Post-Doctoral Researcher with the Department of Computer, Control, and Management Engineering (DIAG), Sapienza University of Rome. He visited LIRMM, Montpellier, as an Intern, in 2014, and he was a Visiting Ph.D. Student with CNRS-IRISA in 2018. Throughout his Ph.D. and the subsequent post-doctoral experience, he worked on vision-based control and estimation methods for humanoid and surgical robots, with a focus later on scientific and technological problems in the medical robotics domain.

Claudio Pacchierotti (Senior Member, IEEE) received the Ph.D. degree from the University of Siena in 2014. He has been a tenured Researcher with CNRS-IRISA, Rennes, France, since 2016. He was previously a Post-Doctoral Researcher with Italian Institute of Technology, Genoa, Italy. He was a Visiting Researcher with the Penn Haptics Group, University of Pennsylvania, in 2014, the Department of Innovation in Mechanics and Management, University of Padua, in 2013, the Institute for Biomedical Technology and Technical Medicine (MIRA), University of Twente, in 2014, and the Department of Computer, Control and Management Engineering, Sapienza University of Rome, in 2022. He received the 2014 EuroHaptics Best Ph.D. Thesis Award and the 2022 CNRS Bronze Medal. He is the Senior Chair of the IEEE Technical Committee on Haptics, the Co-Chair of the IEEE Technical Committee on Telerobotics, and the Secretary of the Eurohaptics Society.